The Astrophysical Journal, 719:1385–1392, 2010 August 20 doi:10.1088/0004-637X/719/2/1385

WHITE LIGHT AND IN SITU COMPARISON OF A FORMING MERGED INTERACTION REGION

A. P. Rouillard[1,2,7], B. Lavraud[1,2], N. R. Sheeley[3], J. A. Davies[4], L. F. Burlaga[5], N. P. Savani[6], C. Jacquey[1,2], and R. J. Forsyth[6]

[1] Centre d'Etude Spatiale des Rayonnements, Université de Toulouse, 21028, Toulouse, France; arouilla@gmu.edu
[2] Centre National de la Recherche Scientifique, UMR 5187, Toulouse, France
[3] Space Science Division, Naval Research Laboratory, Washington, DC 20375-5352, USA
[4] Space Science and Technology Department, Rutherford Appleton Laboratory, Chilton, OX11 0QX, UK
[5] Goddard Space Flight Center, Greenbelt, MD 20771, USA
[6] Blackett Laboratory, Imperial College London, London, SW7 2BW, UK
Received 2010 January 12; accepted 2010 June 4; published 2010 July 29

ABSTRACT

The images taken by the Heliospheric Imager (HI) instruments, part of the *SECCHI* imaging package on board the pair of *STEREO* spacecraft, provide information on the radial and latitudinal evolution of the plasma transported by coronal mass ejections (CMEs). In this case study, a CME, appearing near 15 UT on 2007 November 15 in *SECCHI* coronagraph images, leads to the formation of two out-flowing density structures (DSs) in the heliosphere. The analysis of time-elongation maps constructed from images obtained by the HI instruments shows that these DSs were propagating along the Sun–Earth line. A direct comparison of HI images and in situ measurements taken near Earth could therefore be performed. These two DSs are separated by a cavity associated with little brightness variation or equivalently little electron density variation. In situ measurements made in the solar wind near Earth on 2007 November 20 show that this cavity corresponds to a magnetic cloud (MC). While the leading DS is related to the sheath in front of the MC, the second DS is located on the sunward side of the MC where high-speed solar wind from a coronal hole catches up and interacts with the MC. We conclude that HI observes the sub-structures of a merged interaction region (MIR), a region of the interplanetary medium where the total solar wind pressure is greatly enhanced by the interaction of an MC with the ambient solar wind. This MIR caused the largest geomagnetic storm in 2007.

Key words: solar–terrestrial relations – solar wind – Sun: coronal mass ejections (CMEs)

1. INTRODUCTION

The solar wind speed measured near the Earth can vary from low (∼300–400 km s^{-1}) to high values (∼600–700 km s^{-1}) in a matter of hours. This rapid variation can be the result of solar rotation bringing sources of fast and slow solar winds at adjacent longitudes into radial alignment, allowing, on occasion, fast solar wind to catch up and interact with the slow solar wind during its outward expansion. Such stream interaction regions (SIRs) are usually associated with high values of the sum of the magnetic pressure and plasma pressure (Burlaga & Ogilvie 1970; Jian et al. 2006). When an SIR is observed over two or more consecutive solar rotations (separated by ∼27 day intervals), it is called a corotating interaction region (CIR). High-speed streams can also entrain slow solar transients forming "merged interaction regions" (MIRs) with strong magnetic fields at 1 AU (>30 nT). MIRs can strongly influence geomagnetic and ionospheric activity (Burlaga et al. 1991, 2003; Fenrich & Luhman 1998). For instance, for a north–south magnetic flux rope, the compression of the flux rope by a CIR leads to an intensification of the southward pointing magnetic field in the rear portion of the cloud, which combined with a preconditioning effect of the magnetosphere by a prior northward magnetic field period, can make the transient more geoeffective (Lavraud et al. 2006). Interaction regions at 1 AU may occur without coronal hole associated high-speed streams such as in the sheaths behind transient shocks or ahead of fast solar ejecta (Burlaga et al. 1981, 2003; Sheeley et al. 1985). Much is known about the propagation of MIRs beyond 1 AU from comparison of in situ measurements at 1 AU with data taken further out in the heliosphere by spacecraft such as *Voyager* (Burlaga et al. 1986). However, relatively little is known about the structure and formation of MIRs inside 1 AU; this is the subject of this paper.

2. OBSERVATIONS BY THE *SECCHI* EXPERIMENT

On 2006 October 25, NASA launched *STEREO* which consists of two spacecraft. Each spacecraft used close flybys of the moon to escape into heliocentric orbits near 1 AU, with one spacecraft trailing Earth (*STEREO-BEHIND* or *ST-B*) and the other leading Earth (*STEREO-AHEAD* or *ST-A*; Kaiser 2005; Kaiser et al. 2008). Along with a comprehensive complement of in situ instrumentation, each spacecraft carries a suite of imagers—the *SECCHI* package (Howard et al. 2008). *SECCHI* consists of an Extreme Ultraviolet Imager (EUVI), two coronagraphs (COR-1 and COR-2), and two Heliospheric Imagers (HIs). The HI instruments are described in detail by Eyles et al. (2009) and Brown et al. (2009).

Figure 1(a) presents a view of the ecliptic plane from solar north on 2007 November 17 showing the relative positions of *ST-A*, *ST-B*, the Earth (E), and the near-Earth *Advanced Composition Explorer* (*ACE*; Stone et al. 1998). The elongation extents in that plane of the fields of view (FOV) of the inner HI-1 and outer HI-2 cameras on *STEREO-A* (termed HI-1A and HI-2A, respectively) are shown as dot-dashed and solid black lines, respectively. The extents of the FOV of HI-1A and HI-2A out of the ecliptic plane are shown in Figure 1(c), with the same line styles as in Figure 1(a). Figures 1(b) and (d) present analogous schematics for *ST-B*. The elongation, α, of a transient T in the solar wind as observed by either of the *STEREO* spacecraft is defined as the Sun–spacecraft–T angle, being zero

[7] Current address: College of Science, George Mason University, Fairfax, VA 22030, USA.

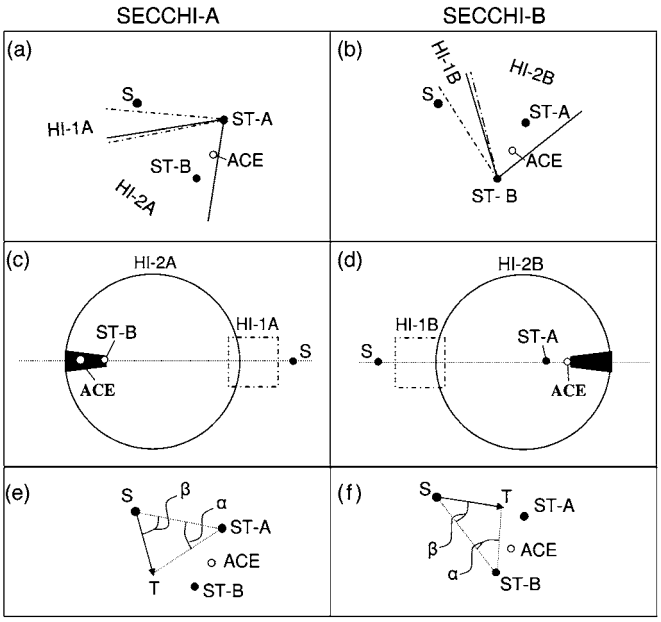

Figure 1. Panels (a) and (b): views of the ecliptic plane from solar north on 2007 November 17 showing the relative positions of *STEREO-A* (*ST-A*), *STEREO-B* (*ST-B*), and the Earth (E) as well as the extents of the HI-1/2 FOVs in the ecliptic plane separately for *STEREO-A* and *STEREO-B*. Panels (c) and (d): the extents of the FOVs of HI-1/2A and HI-1/2B out of the ecliptic plane. Panels (e) and (f) are the same as panels (a) and (b) but showing the angular coordinate system used in this paper and without the FOVs.

at Sun center. Figures 1(e) and (f) present a view of the ecliptic from solar north, like Figures 1(a) and (b) discussed already, illustrating the angular coordinate system used in this paper. The angular separation between the Sun–spacecraft line and the direction of propagation of the transient T, β, equates to the longitude separation in an ecliptic-based heliocentric coordinate system ($\Delta\phi$) when the transient propagates in the ecliptic plane.

The term "coronal mass ejection" (CME) is widely used to describe ejections of solar plasma observed in coronagraph images. The causes of the changes of a CME's appearance in white light observations as it moves away from the Sun are still poorly understood and could be the result of a wide range of physical processes (e.g., Lugaz et al. 2008). In the present paper, we use the term CME to describe coronal brightness variations observed in the COR-2 images. Brightness variations observed in difference images obtained outside the coronagraph FOV are referred to as "density structures" (DSs) and, as we shall see in this paper, can result from other processes than simply the ejection of solar plasma into the interplanetary medium.

A CME was launched on 2007 November 15, appearing as a halo mass ejection in images from COR-2A and LASCO C2 images and as a partial halo mass ejection in COR-2B images. Signatures of the CME could be clearly followed through the COR-2B FOV and out to the Earth-like distances imaged by HI-2B. Figure 2 presents running difference images from HI-2B (left-hand column) and HI-2A (right-hand column) showing DSs, associated with the CME, approaching the elongation of Earth (E) as well as *ST-A* and *ST-B*, respectively. Running difference images, obtained by subtracting the preceding image from the current one, are particularly useful as they reveal faint features that are propagating through the FOV.

Two additional CME-like structures could be identified in the COR-2 images but become very faint at the times of the observations shown in Figure 2. These CMEs (now referred to as CME-1 and CME-3) had very different trajectories to the halo mass ejection analyzed in this paper (now referred to as CME-2). The first DS of CME-2 to appear in the HI-2B FOV originates in COR-2 as the outer edge of CME-2 (and is labeled as "DS 1" in this figure). A second smaller trailing DS ("DS 2") appeared in the HI-2B FOV near the time of Figure 2(a) and grew rapidly into an extensive structure (Figures 2(b) and (c)). This trailing DS propagates with DS 1 to the outer edge of the HI-2B camera and appears to sweep over the Earth. As we shall determine in the next section, the same two DSs are also present in HI-2A running difference images (DSs 1 and 2 in Figures 2(d–f)), albeit fainter such that DS 2 in particular is not very well defined. Nevertheless, these two structures appear to sweep over the Earth in both the HI-2A and HI-2B images. This could simply be a result of perspective; the longitude of propagation of DSs 1 and 2 relative to the observer could be such that they actually pass behind or in front of the Earth or either of the *STEREO* spacecraft. The following analysis removes this ambiguity and shows that these two DSs do indeed pass over the Earth.

3. DETERMINING THE TRAJECTORY OF THE CME PARTS

Figure 3(a) presents a J-map created by extracting the intensity variation along a solar radial corresponding to a constant position angle (PA) of 90° from a series of HI-1/2A composite difference images, and plotting this as a function of elongation (*Y*-axis) and time (*X*-axis; Sheeley et al. 1999, 2008a, 1999, 2008b; Davies et al. 2009). Figure 3(c) presents a J-map, in the same format, created along P.A. = 270° from HI-1/2B composite images. The first series of tracks in the HI-1/2A J-map (panel (a)) appear to converge. It has been shown that converging tracks form in J-maps constructed from HI-1/2A images when a CIR transits through the combined HI-A FOV (Rouillard et al. 2008, 2010a, 2010b; Sheeley et al. 2008a, 2008b). These converging tracks have been related to different "blobs" (e.g., small mass ejections) that are swept up by high-speed streams (e.g., Rouillard et al. 2009a, 2010b).

DSs 1 and 2 associated with CME-2 produce a pair of nearly parallel tracks in each J-map and are clearest in the *ST-B* observations (in particular DS 2). The tracks appear to gradually accelerate/decelerate (negative acceleration) during their transit to 1 AU. Rouillard et al. (2008, 2009a, 2009b) and Sheeley et al. (2008a, 2008b) have shown that the apparent acceleration of transients at the elongations imaged by HI J-maps is largely an effect of projection geometry. The elongation variation, $\alpha(t)$, of a point in the solar wind depends upon its radial speed, V_r, and the angle β (or equivalently $\delta = 90^\circ - \beta$):

$$\alpha(t) = \mathrm{atan}\left[\frac{V_r t\ \sin\beta}{r_{A/B}(t) - V_r t\ \cos\beta}\right], \qquad (1)$$

where $r_{A/B}$ is the radial distance of *ST-A*/*B*. Values of β and V_r can be obtained from the elongation variation recorded by HI, thereby providing an estimated trajectory and velocity for the transient. Figures 3(b) and (d) present the calculated $\alpha(t)$ variations which fit the observed tracks most closely. Calculated values of β and V_r for all tracks are presented in Table 1.

The values of β listed in Table 1 suggest that the trajectories of DS 1 and DS 2 are less than 10° off the Sun–Earth line. The tracks of DSs 1 and 2 in J-maps from *ST-B* (Figure 1(c)) are the clearest and probably give the most reliable fits. No

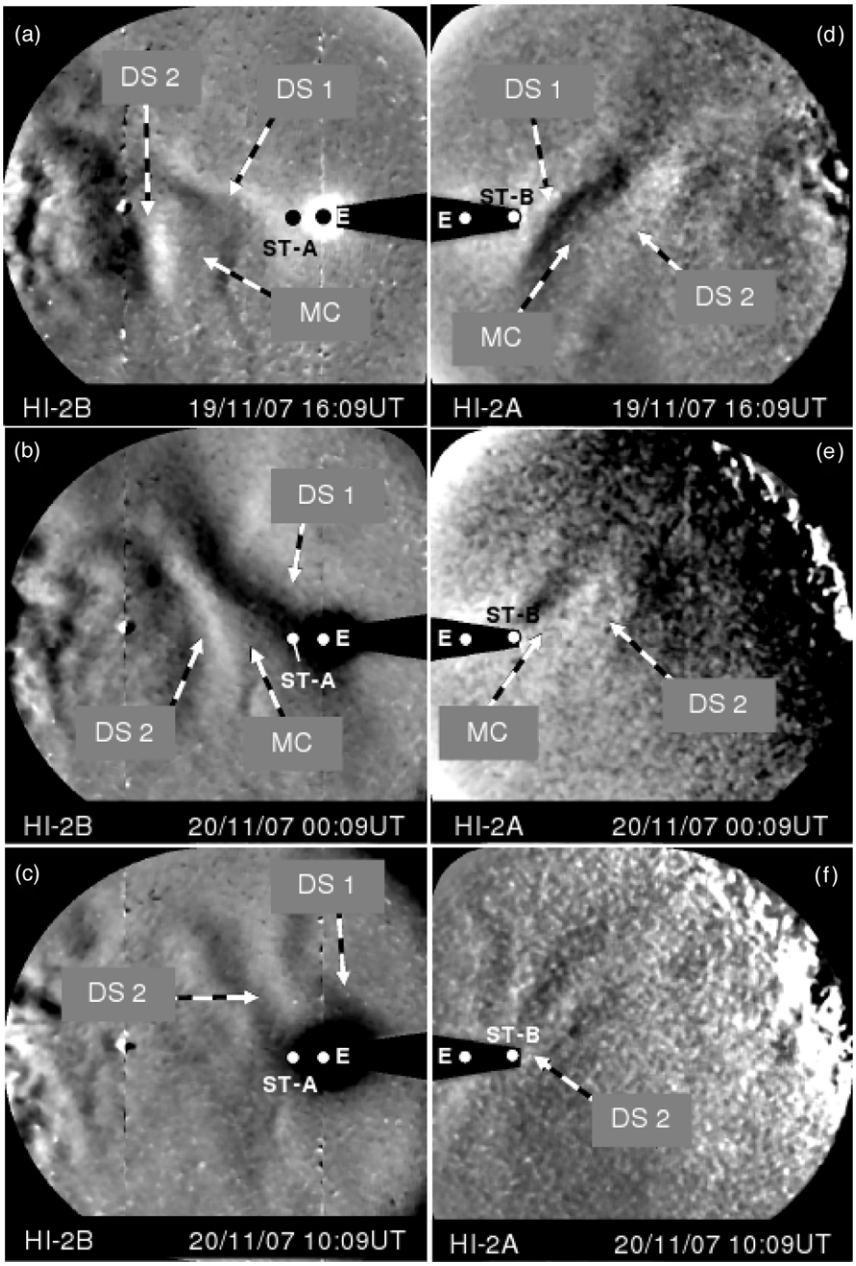

Figure 2. Sequence of running difference images from HI-2B (left-hand panels) and HI-2A (right-hand panels) around the times when the DSs of CME-2 impacted the Earth. DSs 1 and 2 are marked. The location of the MC inferred from *ACE* observations is also shown.

appreciable speed difference is found between DS 1 (395 ± 18 km s^{-1}) and DS 2 (391 ± 14 km s^{-1}) from *ST-B* J-maps. We discuss this finding later in this paper. Averaging the β values obtained for DSs 1 and 2 gives $\overline{\beta} = 23^\circ \pm 7^\circ$ relative to *ST-B* and $\overline{\beta} = 15^\circ \pm 10^\circ$ relative to *ST-A*. If one assumes that the DSs observed by the HIs have a longitude width of at least $\sim 10^\circ$, these $\overline{\beta}$ values show that DSs 1 and 2 seen by HI-A and HI-B are the same structures and that they should have impacted Earth.

The values of β listed in Table 1 can be used to determine which of the converging tracks are associated with the same CIR by assuming that the CIR is corotating at the solar rotation period of 27 days. The speeds estimated from the CIR tracks observed by HI-A are similar and the average is $\bar{V} \sim 335 \pm 25$ km s^{-1} but the β angles decrease progressively ($86^\circ \pm 7^\circ$, $65^\circ \pm 7^\circ$, and $45^\circ \pm 9^\circ$); this decrease is a consequence of the CIR gradually approaching the Sun–*ST-A* line (e.g., Rouillard et al. 2010a). The tracks associated with this CIR are plotted as dotted lines in Figures 3(b) and (d); the three-dimensional trajectory of each of these CIR tracks originated near the northwestern boundary of a low-latitude hole observed in *STEREO* extreme ultraviolet images. Coronal holes are well-known sources of high-speed streams and we suggest that the CIR formation is related to the presence of this hole.

The tracks that originate on the leading edge of CME events observed in COR-2 images are shown as solid lines (namely, CME-1, CME-2 (DS 1), and CME-3). The source regions of the DS of CME-1 and DS 2 of CME-2 were also found to originate near the western boundary of the coronal hole; CME-1 ($V = 452 \pm 40$ km s^{-1}) was propagating faster than the CIR ($\sim 335 \pm 25$ km s^{-1}). However, the rear of CME-2 (DS 2) was propagating with a similar speed ($\bar{V} \sim 357 \pm 27$ km s^{-1}: the average value of V from HI-A and HI-B observations of DS 2)

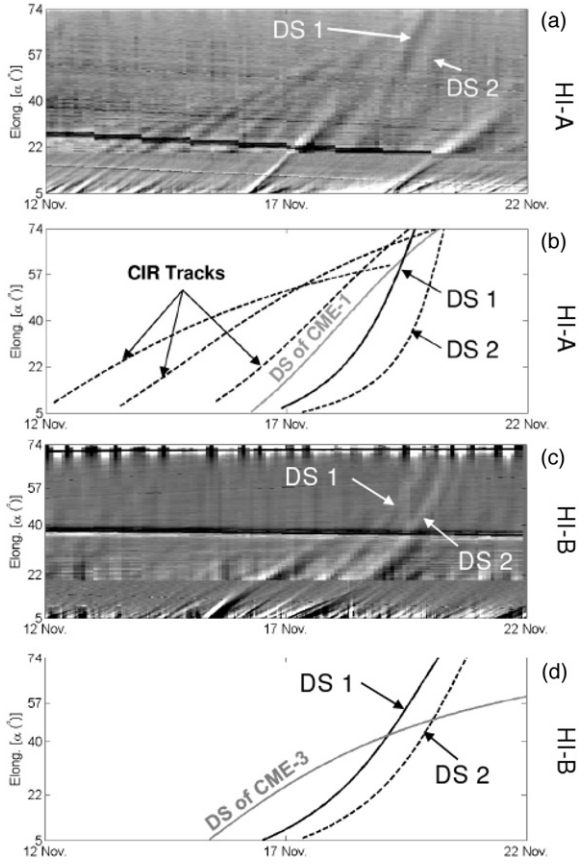

Figure 3. J-maps constructed from running difference images taken by HI-1 (α ranging from 4° to 18°) and HI-2 (α beyond 18° up) on *ST-A* (a) and *ST-B* (c). The fitted tracks obtained using Equation (1) plotted in a J-map format for *ST-A* (b) and *ST-B* (d) observations. The solid tracks are associated with CMEs. The dotted tracks are associated with compression of plasma in the CIR. Note that DS 2 is a dotted track because the CIR compressed plasma on the sunward edge of the MC.

Table 1
Obtained Best-fit Longitude β and Speed V_r for the Tracks Shown in Figures 3(b) and (d)

Label	V_r (km s^{-1})	β(°)	IMPACT?
Results of HI-1/2A:			
CIR-1	337 ± 35	86 ± 7	NO
CIR-2	335 ± 20	65 ± 7	NO
CIR-3	330 ± 22	45 ± 9	*ST-B*
CME-1	452 ± 40	50 ± 15	*ST-B*
CME-2 (front)	402 ± 20	17 ± 10	*ST-B/ACE/ST-A*
CME-2 (rear)	323 ± 40	12 ± 10	*ST-B/ACE/ST-A*
Results of HI-1/2B:			
CME-3	347 ± 72	90 ± 23	NO
CME-2 (front)	395 ± 18	26 ± 9	*ST-B/ACE/ST-A*
CME-2 (rear)	391 ± 14	21 ± 5	*ST-B/ACE/ST-A*

Notes. The predicted impacts of each listed DS at *ST-B*, *ACE*, and/or *ST-A*, by assuming that a DS has a longitudinal width of ∼45°, are provided in the last column.

than the CIR and could have been caught up by high-speed streams during its transit to 1 AU.

Figure 4(a) presents a schematic showing the in-ecliptic position of the various structures that formed the tracks in HI J-maps. CME-1 is propagating with a longitude separation of only 10° relative to *ST-B* while CME-3 propagated some 50° westward and south of *ST-A* (i.e., outside the HI-1/2A FOV). Cane et al. (1997) noted that remarkably few interplanetary CMEs (ICMEs) have been observed by pairs of spacecraft even separated by only 40° in longitude and concluded that ICMEs typically extend over 40°–50° in longitude, similar to the average latitudinal extent of CMEs observed in coronagraphs (St. Cyr et al. 2000). If we assume a longitudinal width of ∼45° centered at its longitude of propagation, then we predict that CME-1 should impact *ST-B* a few hours before DS 1, but should probably not impact *ACE* (see Column 5 of Table 1). DSs 1 and 2 (CME-2) may impact all three spacecraft while CME-3 should miss all three spacecraft.

Despite CME-2 propagating near the Sun–Earth line (i.e., between *ST-A* and *ST-B*), HI-A and HI-B observed very different brightness variations. Thomson scattering forces geometrical constraints on the part of the solar wind that HI can observe and which can account for some of the observational differences between HI-A and HI-B (Billings 1966). The combination of Thomson scattering effects with the fall off with radial distance of both the incident solar electromagnetic radiation and the solar wind density is such that scattered light is maximized at points located on a sphere of which the Sun-spacecraft segment is a diameter. This sphere was called the Thomson sphere by Vourlidas & Howard (2006) and is also described in great detail in Howard & Tappin (2009).

Equicontours of the values of coronal brightness relative to the maximum brightness (Thomson sphere) are plotted in Figure 5 for the different lines of sight recorded by *ST-A* and *ST-B* in the ecliptic plane. In this figure, the contour level equal to 1 is the intersection of the Thomson sphere with the solar ecliptic plane. The position of the Sun (S) and the *ST-A* and *ST-B* spacecraft (A/B) are also shown; we remind the reader that HI-1/2A observes the corona off the East limb of the Sun while HI-1/2B observes the corona off the West limb (see Figures 1(c) and (d)). To compare *ST-A* and *ST-B* observations on the same Thomson sphere, the two spacecraft are placed at the same point (A/B); their actual orbital positions in the ecliptic plane are shown in Figure 1. As we can see, electrons located around the Thomson sphere contribute most to the light detected by HI-A and HI-B. In contrast, electrons situated along the Sun–observer (A/B) line contribute very little to the recorded brightness.

Black and white arrows show the directions of propagation of CME-2, determined separately from HI-A ($\overline{\beta} \sim 15° \pm 10°$) and HI-B ($\overline{\beta} \sim 23° \pm 7°$) observations and obtained by averaging the β values of DS 1 and DS 2 given in Table 1. The DSs of CME-2 were propagating well inside the Thomson sphere and were therefore poorly resolved by the HIs at small elongation angles. These equicontours suggest that the DSs should only become apparent when they reach the Thomson sphere at large elongation angles ($\alpha > 40°$); this effect would be particularly strong in HI-A observations because the DSs were propagating at smaller β angles relative to *ST-A* ($\overline{\beta} \sim 15° \pm 10°$) than relative to *ST-B* ($\overline{\beta} \sim 23° \pm 7°$). This observational constraint is confirmed by the *ST-A* J-map; the DSs become clear beyond $\alpha = 40°$ (Figure 3(a)). In contrast, the DSs are already visible at $\alpha = 20°$ in HI-B observations because the DSs approach the Thomson sphere at these smaller elongation angles.

DS 2 observed from *ST-B* left the clearest and broadest signal with strong brightness variations already evident at $\alpha \sim 20°$. We relate this latter effect to the interaction between CME-2 and the background solar wind for the reasons we describe here. When solar wind transients are entrained and compressed by

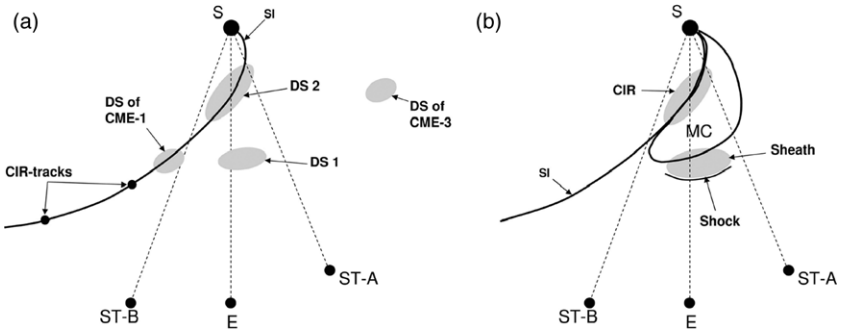

Figure 4. Panel (a): view of the ecliptic from solar north on 2007 November 17 showing the position of two blobs entrained by the CIR (CIR tracks in Figure 3) and which are not associated with the three CMEs. The CIR SI is the black spiral rooted at the Sun (S). The position of DSs associated with the three CMEs identified in Figures 2 and 3 are also shown in gray. Panel (b): the same as (a), with the HI observations of DSs 1 (sheath) and 2 (interaction region) shown along with the position of the shock and the MC inferred from in situ observations.

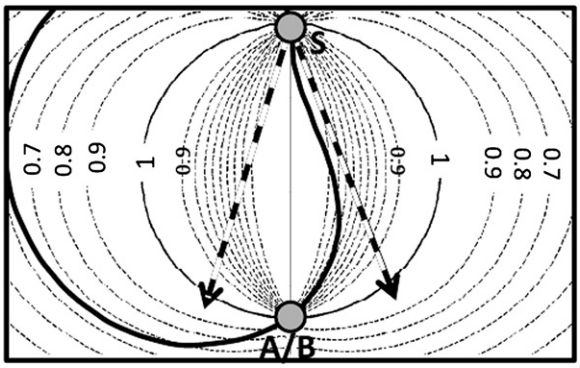

Figure 5. View of the solar equatorial plane from solar north with the position of the Sun (S) and the *ST-A* and *ST-B* spacecraft (A/B) placed at the same location to compare their Thomson spheres. Equicontours of the values of coronal brightness relative to the maximum brightness (Thomson sphere) for the different lines of sight recorded by *ST-A* and *ST-B* in the ecliptic plane. The locus of edge-on views of the CIR density spiral is shown as continuous thick black curve. The directions of propagation of DS 1 and DS 2 of CME-2, obtained by averaging the longitudes of propagation (βs), calculated from HI-A ($\overline{\beta} \sim 15^\circ \pm 10^\circ$) and HI-B ($\overline{\beta} \sim 23^\circ \pm 7^\circ$) observations, are shown on this map by black and white arrows.

high-speed streams, the compression region tends to be aligned with the plane of the stream interface which is the boundary between fast and slow solar winds. Equivalently, a vector normal to the surface of compression tends to be normal to the local tangent to the Parker spiral (e.g., Rouillard et al. 2009a). A white light imager integrates light along the line of sight and should integrate more light when it observes a compression region edge-on (i.e., extending along the line of sight) rather than face-on (i.e., extending across the line of sight). The "locus of enhanced visibility," tracing the locus of edge-on views of the Parker spiral in polar coordinates, is a "bean-shaped curve" which has a strong east–west asymmetry as viewed from an observer at 1 AU (Sheeley & Rouillard 2010). This curve is plotted as a black line in Figure 5; the east–west asymmetry means that HI-A (looking off the East limb) and HI-B (looking to the West limb) will observe the spiral differently at similar elongation angles; *ST-A* will observe the spiral edge-on outside the Thomson sphere while *ST-B* observes the spiral edge-on inside the Thomson sphere. Sheeley & Rouillard (2010) were able to explain a whole range of HI observations related to the compression of streamer blobs by considering the effect of the Thomson sphere together with the effect of the spiral. Figure 5 shows that the averaged trajectory of DSs 1 and 2 relative to ST-B follows the black curve until it reaches the Thomson sphere, therefore any interaction between CME-2 and a CIR which would increase density along the CIR spiral would increase the white light signature of the sunward edge of CME-2 (DS 2) in HI-B images but not in HI-A images, as observed.

We now present the in situ measurements which confirm impacts of DSs 1 and 2 at *ACE* and that a strong interaction developed between the CIR and CME-2.

4. IN SITU MEASUREMENTS

Figure 6 presents the in situ measurements of the solar wind at the time when DSs 1 and 2 appeared to sweep over the Earth in HI-2A/B images (Figure 2). The arrival of DS 1 is associated with an increase in solar wind density from 4 cm^{-3} to 20 cm^{-3} (a). The WIND measurements of the proton density (Ogilvie et al. 1995) are also plotted as a black line in Figure 6(a) and show that these WIND and *ACE* measurements are consistent. This high DS is immediately followed by a smooth increase in the magnetic field strength (b) associated with a continuous rotation in both the magnetic field azimuth (c) and elevation (d). The temperature (f) and plasma beta (g) are lower in this region than in the high-density region in DS 1. Due to the lack of alpha and electron particle data for some of the L1 *ACE* data, the total perpendicular pressure calculated from *ACE* data (gray line in Figure 6(h)) was also calculated using the WIND spacecraft measurements of the temperature and density of the solar wind electron, proton, and alpha particles (Ogilvie et al. 1995) and is shown as a black line in Figure 6(h). The pressure calculated from WIND tends to be a little greater than from *ACE* because alpha particles were not included in the *ACE* pressure calculation as there were too many data gaps during this time interval. The variations of the plasma moments and magnetic fields measured after the passage of DS 1 are characteristic of the passage of a magnetic cloud (MC; Burlaga et al. 1981; Klein & Burlaga 1982). An MC was defined by Burlaga et al. (1981) as a region of enhanced magnetic field strength, smooth rotation of the magnetic field vector, and low proton density and temperature. The leading edge of DS 1 observed at *ACE* forms a shock. We therefore associate DS 1 with the sheath of the MC—an interaction region between the MC and the leading shock.

White light difference images record changes in brightness associated with variations in coronal electron density; therefore MCs cannot be observed directly in white light. However, the lower ion density inside the MC should be associated with an extended region of lower coronal brightness variation. Such a region is observed in HI-2 images from both *ST-A* and *ST-B* between DSs 1 and 2 (see Figure 2).

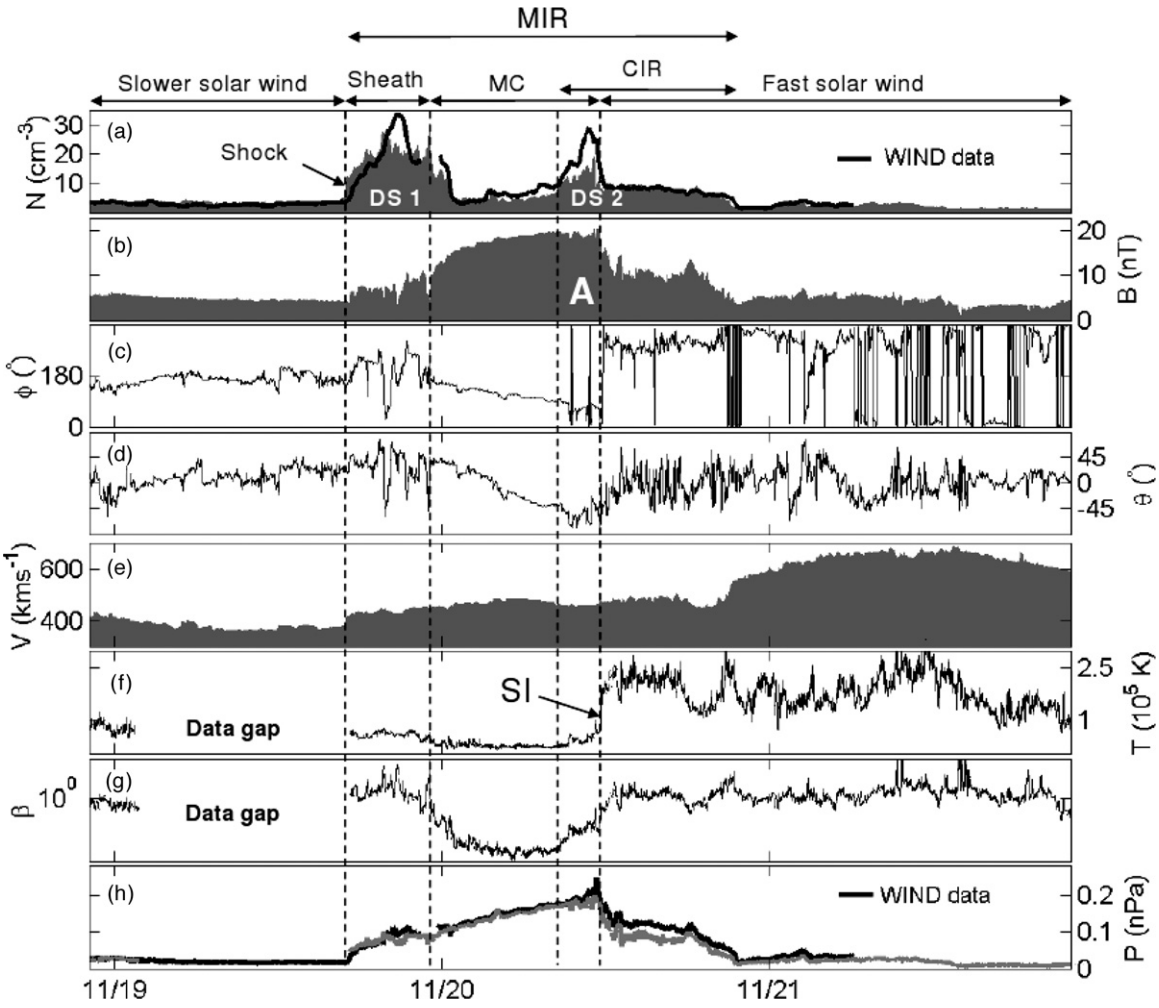

Figure 6. In situ data measured during the passage of CME-2 and the following high-speed streams. The solar wind proton density (*N*) measured by the *ACE* and WIND spacecraft are shown in (a) as a shaded gray area and a black line, respectively. The *ACE* measurements of the magnetic field strength (*B*), azimuth (ϕ), and elevation angles (θ) are all shown in (b), (c), and (d), respectively. The speed (*V*), temperature (*T*), and plasma beta (β) derived from *ACE* solar wind proton data are shown in (e), (f), and (g), respectively. Panel (h) presents the total pressure (*P*) calculated from *ACE* proton data (and assuming charge neutrality for the electrons) and plotted as a gray line as well as *P* calculated from WIND proton, electron, and alpha particle data and plotted as a black line. Dashed vertical lines bound the sharp density increases of the sheath and region "A." The passage of the stream interface is marked by the last of these four vertical lines. Region A is a region of dense plasma inside the deformed part of the MC.

After the passage of the MC, DS 2 sweeps over the Earth. This is associated with an increase in in situ density from ∼5 cm^{-3} to ∼15 cm^{-3} (a). Midway through the passage of DS 2 an increase in solar wind speed (e) and temperature is observed (f) which marks a stream interface. These high temperatures and speeds, which last beyond November 21, are associated with the passage of high-speed streams which compress plasma located behind the MC by forming an interaction region. The passage of this high-speed stream is measured by *ACE* 27 days earlier on 2007 October 25 and 27 days later on 2007 December 18, this interaction region is therefore part of a CIR event. After the passage of the stream interface, the average azimuth angle of the magnetic field is 315°. This polarity corresponds to that of the low-latitude coronal hole identified as the source region of the high-speed streams which led to the CIR formation. This CIR, evidence for which is observed in the HI-A J-maps, was predicted to sweep over the two *STEREO* spacecraft and *ACE* at the same time as DS 2. This is here confirmed at *ACE* by the analysis of the in situ data. Figure 4(b) is a repeat of Figure 4(a), showing the location of the shock, the sheath (DS 1), the MC, the stream interface (SI), and the CIR (DS 2) derived from in situ measurements.

5. DISCUSSION

Magnetic field strength is expected to peak at the center of magnetic flux ropes which possess force-free geometry (Burlaga 1988). This is not observed for this MC (Figure 6(b)). The variation of the field strength is asymmetric relative to the center of the rope, peaking at the end of the MC passage (i.e., the sunward edge of the MC). The deviation of the magnetic field distribution from force-free field geometry is here related to compression effects occurring mainly at the rear of the MC. This peak in magnetic field strength occurs inside a region of relatively dense plasma (∼15 cm^{-3} for 3 hr). The in situ data suggest that the intensification of DS 2 is largely related to the compression on the sunward side of the MC. Note that DS 2 is a combination of a region inside the MC (A in Figure 6) and the compressed plasma between the MC and the high-speed stream. The high-density region A is the CIR compression region impinging into the MC.

The front parts of MCs usually move some 30–40 km s^{-1} faster than the rear parts (Klein & Burlaga 1982); this is attributed to the self-similar expansion of the MC (Klein & Burlaga 1982; Lepping et al. 2008; Démoulin & Dasso 2009).

Recently, Rouillard et al. (2009b) and Savani et al. (2009) have measured this expansion in white light images of CMEs where the DSs on the leading and trailing parts of a flux rope could be identified unambiguously. These authors confirmed a typical expansion rate of $\sim$30 km s^{-1}. At *ACE*, the in situ measurements reveal that the front and rear of the MC associated with CME-2 were both moving with a speed of 410 km s^{-1} which agrees within errors with the speeds estimated from the J-map analysis. Self-similar expansion of the MC was therefore prohibited by the compressive effects of this high-speed stream as early as when it entered the HI-2B FOV.

The combination of DS 1 (sheath region), the MC, and the interaction region between the MC and the high-speed stream (CIR) forms a continuous region of high total pressure (h) corresponding to an MIR (Burlaga et al. 2003). This region results directly from the MC compressing the slower solar wind ahead (forming the sheath) and the interaction of the back of the MC with high-speed streams. We therefore suggest that in HI images DSs 1 and 2 are the sub-structures of a forming MIR.

The trailing DS, DS 2, is already clear when it is first evident in the HI-2B difference images ($\alpha \sim 20^\circ$) suggesting that compression may have already started at this elongation. From the direction of propagation of DS 2 inferred from J-maps ($21^\circ \pm 5^\circ$ relative to *ST-B*) and the elongation of the sunward edge of HI-2B ($\alpha \sim 20^\circ$), we infer that interaction between the CIR and the MC may have already started at 0.5 AU from the Sun.

In this paper, we have concentrated on interpreting the HI observations of two DSs propagating toward *ACE* and have intentionally ignored the *ST-A* and *ST-B* in situ data. We leave this analysis to other studies, noting that the DSs from CME-1 and CME-2 were predicted to impact *ST-B* and two density enhancements separated by MCs are indeed observed in situ at *ST-B*. Because of the proximity of the DSs of CME-1 and CME-2 in longitude and their similar speeds, it may be that CME-1 is actually the eastern boundary of the MC associated with CME-2, perhaps interacting with the CIR and thus visible from *ST-A*. We will tackle this remaining ambiguity by a full modeling of the corona in a future paper. At *ST-A*, only DSs of CME-2 should have been observed in situ and this is confirmed by the passage of an MC with the same chirality as the flux rope observed at *ACE*.

6. CONCLUSION

A simple analysis of a halo mass ejection from the Sun to 1 AU provided some insights into the propagation of CMEs in a structured solar wind. The analysis of white light images using the J-map technique predicted that most of the plasma transported by this halo mass ejection should be propagating between the longitude of *ST-B* and *ST-A*.

The analysis of J-maps alone suggests that the CME interacts with a CIR during its transit to 1 AU. Inference of this interaction was based on two different observations. First, a CME–CIR interaction was inferred from a kinematic analysis of the progression, in the HI-A FOV, of the leading edge of a CIR (compression of blobs) and the estimated trajectory and speed of the DSs of the CME (the result of which is shown in Figure 5). Second, by noticing that the rear of CME-2 (DS 2) observed by HI-B was the broadest and clearest feature of all the DSs observed either in HI-A or HI-B. This latter observation is strongly suggestive that HI-B is offering an edge-on view of the formation of a compression region at the rear of CME-2. The existence of this compression region is confirmed by the 1 AU in situ measurements made by the *ACE* and WIND spacecraft.

It is interesting to note that the rear of the MC sweeps over the Earth and *ST-A* and *ST-B*; the HI-2A and HI-2B cameras provide a view of the flux rope from inside (see central panels of Figure 2). The propagation of the CME near the Sun–Earth line led to an association between the white light features and the dense plasma on the boundary of the MC observed by *ACE*. The magnetic field of the MC pointed first northward and then southward as *ACE* propagated toward the compressed rear of the MC (DS 2). The impact of this enhanced southward interplanetary magnetic field led to the strongest geomagnetic storm in 2007; the *Dst* index dropped below -70 nT at 20 UT on 2007 November 20 at the time of passage of DS 2.

This and other recent studies using *STEREO* observations (Rouillard et al. 2009b; Davis et al. 2009; Möstl et al. 2009; Wood & Howard 2009) show that the location of the flux ropes ejected during some CMEs can be estimated from white light images. In the not-too-distant future, we may therefore be in a position to predict the orientation and location of flux ropes of CMEs in white light images and infer from J-maps if the CME was caught up by high-speed streams during its transit from the Sun to 1 AU. Such an achievement would be of critical importance for space-weather predictions.

The *STEREO*/*SECCHI* data are produced by a consortium of RAL (UK), NRL (USA), LMSAL (USA), GSFC (USA), MPS (Germany), CSL (Belgium), IOTA (France), and IAS (France). The *ACE* data were obtained from the *ACE* science center. The WIND data were obtained from the Space Physics Data Facility (SPDF). The *SECCHI* images were obtained from the World Data Center, Chilton, UK.

REFERENCES

Billings, D. E. 1966, A Guide to the Solar Corona (San Diego, CA: Academic Press)
Brown, D. S., Bewsher, D., & Eyles, C. J. 2009, Sol. Phys., 254, 185
Burlaga, L. F. 1988, J. Geophys. Res., 93, 7217
Burlaga, L., Berdichevsky, D., Gopalswamy, N., Lepping, R., & Zurbuchen, T. 2003, J. Geophys. Res., 108, SSH2-1
Burlaga, L. F., Hewish, A., & Behannon, K. W. 1991, J. Geophys. Res., 96, 21213
Burlaga, L. F., McDonald, F. B., & Schwenn, R. 1986, J. Geophys. Res., 91, 13331
Burlaga, L. F., & Ogilvie, K. W. 1970, Sol. Phys., 15, 61
Burlaga, L. F., Sittler, E., Mariani, F., & Schwenn, R. 1981, J. Geophys. Res., 86, 6673
Cane, H. V., Richardson, I. G., & Wibberenz, G. 1997, J. Geophys. Res., 102, doi 7075
Davies, J. A., et al. 2009, Geophys. Res. Lett., 36, L02102
Davis, C. J., Davies, J. A., Lockwood, M., Rouillard, A. P., Eyles, C. J., & Harrison, R. A. 2009, Geophys. Res. Lett., 36, L08102
Démoulin, P., & Dasso, S. 2009, A&A, 498, 551
Eyles, C. J., et al. 2009, Sol. Phys., 254, 387
Fenrich, F. R., & Luhmann, J. G. 1998, Geophys. Res. Lett., 25, 2999
Howard, R. A., et al. 2008, Space Sci. Rev., 136, 67
Howard, T. A., & Tappin, S. J. 2009, Space Sci. Rev., 147, 31
Jian, L., Russell, C. T., Luhmann, J. G., & Skoug, R. M. 2006, Sol. Phys., 239, 393
Kaiser, M. L. 2005, Adv. Space Res., 36, 1483
Kaiser, M. L., Kucera, T. A., Davila, J. M., St. Cyr, O. C., Guhathakurta, M., & Christian, E. 2008, Space Sci. Rev., 136, 5
Klein, L. W., & Burlaga, L. F. 1982, J. Geophys. Res., 87, 613
Lavraud, B., Thomsen, M. F., Borovsky, J. E., Denton, M. H., & Pulkkinen, T. I. 2006, J. Geophys. Res., 111, A09208
Lepping, R. P., Wu, C.-C., Berdichevsky, D. B., & Fergusen, T. 2008, Ann. Geophys., 26, 1919
Lugaz, N., Vourlidas, A., Roussev, I. I., Jacobs, C., Manchester, W. B., IV, & Cohen, O. 2008, ApJ, 684, L111
Möstl, C., Farrugia, C. J., Temmer, M., Miklenic, C., Veronig, A. M., Galvin, A. B., Leitner, M., & Biernat, H. K. 2009, ApJ, 705, L180

Ogilvie, et al. 1995, Space Sci. Rev., 71, 55
Rouillard, A. P., et al. 2008, Geophys. Res. Lett., 35, L10110
Rouillard, A. P., et al. 2009a, Sol. Phys., 256, 307
Rouillard, A. P., et al. 2009b, J. Geophys. Res., 114, A07106
Rouillard, A. P., et al. 2010a, J. Geophys. Res., 115, A04103
Rouillard, A. P., et al. 2010b, J. Geophys. Res., 115, A04104
Savani, N. P., et al. 2009, Ann. Geophys., 27, 4349
Sheeley, N. R., Jr., Howard, R. A., Michels, D. J., Koomen, M. J., Schwenn, R., Muehlhaeuser, K. H., & Rosenbauer, H. 1985, J. Geophys. Res., 90, 163
Sheeley, N. R., Jr., & Rouillard, A. P. 2010, ApJ, 715, 300
Sheeley, N. R., Jr., Walters, J. H., Wang, Y.-M., & Howard, R. A. 1999, J. Geophys. Res., 104, 24739
Sheeley, N. R., Jr., et al. 2008a, ApJ, 674, L109
Sheeley, N. R., Jr., et al. 2008b, ApJ, 675, 853
St. Cyr, O. C., et al. 2000, J. Geophys. Res., 105, 18169
Stone, E. C., Frandsen, A. M., Mewaldt, R. A., Christian, E. R., Margolies, D., Ormes, J. F., & Snow, F. 1998, Space Sci. Rev., 86, 1
Vourlidas, A., & Howard, R. A. 2006, ApJ, 642, 1216
Wood, B., & Howard, R. A. 2009, ApJ, 702, 901